

Gravity wave variations during the 2009 stratospheric sudden warming as revealed by ECMWF-T799 and observations

Chihoko Yamashita,^{1,2} Han-Li Liu,¹ and Xinzha Chu²

Received 9 September 2010; revised 11 October 2010; accepted 15 October 2010; published 20 November 2010.

[1] ECMWF-T799 is used to study gravity wave (GW) variations during the 2009 stratospheric sudden warming (SSW) in the Arctic. The magnitude and occurrence of GWs correlate with the location and strength of the polar vortex that is strongly disturbed by planetary wave (PW) growth. This location dependence on PW phase explains the observed GW variability during SSWs. During the development and the onset of SSW, the zonal-mean GW potential energy density (GW-Ep) increases on January 5 and 15–22 in association with the growth of PW wavenumber 1 and wavenumber 2, respectively. As the initial prominent PW magnitude in the lower mesosphere progresses downward, GW-Ep enhancement also seems to show a corresponding descent from January 5–22. GW-Ep peaks before the wind reversal occurrence and significantly weakens after the SSW. These variations are confirmed by COSMIC/GPS observations. Lidar data from Antarctica are also used to validate GWs as derived in ECMWF. **Citation:** Yamashita, C., H.-L. Liu, and X. Chu (2010), Gravity wave variations during the 2009 stratospheric sudden warming as revealed by ECMWF-T799 and observations, *Geophys. Res. Lett.*, 37, L22806, doi:10.1029/2010GL045437.

1. Introduction

[2] Stratospheric sudden warmings (SSWs) have significant influences on the atmospheric circulation from the troposphere to the lower thermosphere [Liu and Roble, 2002]. Although the enhancements of planetary waves (PWs) are considered as the main driver for the generations of SSWs, gravity waves (GWs) play an important role in driving the cooling and warming in the mesosphere and lower thermosphere during SSWs, respectively [Liu and Roble, 2002]. Significant variations of GWs have been observed during SSWs. For example, Rayleigh lidar at Eureka (80°N , 86°W) observed the reduction or enhancement of GW potential energy density (GW-Ep) between 25–55 km during SSWs of the 1992/1993 to 1996/1997 winters [Whiteway and Carswell, 1994; Duck *et al.*, 1998]. Satellite observations revealed the enhancement of zonal-mean GW-Ep during SSWs between 20–35 km and the longitudinal variations of GW-Ep associated with the location of the polar vortex [e.g., Venkat Ratnam *et al.*, 2004; Wang and Alexander, 2009]. The decrease of momentum flux associ-

ated with wind reversal is also observed by HIRDLS during the 2006 SSW [Wright *et al.*, 2010]. While these observational studies indicate the strong variability of GWs associated with SSWs, the physical mechanisms of GW variations are not fully understood. One way to better understand the mechanisms of GW change and the temporal, spatial, and spectral dependence of the GW variation is to conduct detailed analyses of high-resolution models that can at least partially resolve GWs [e.g., Watanabe *et al.*, 2008].

[3] Recently, the European Centre for Medium-Range Weather Forecasts (ECMWF-T799) provides assimilated atmospheric data product with a horizontal resolution Δh of $\sim 0.25^{\circ}$. Owing to the improvement of model resolution, ECMWF-T799 has the potential of partially resolving mesoscale GWs with horizontal scales larger than ~ 100 km. The daily and seasonal variations of resolved GWs in ECMWF-T799 are comparable with SABER observations, though the magnitudes of GWs are a factor of two smaller than SABER observations [Schroeder *et al.*, 2009]. GWs generated by typhoon in ECMWF-T799 agree well with the WRF model and AIRS observations [Kim *et al.*, 2009]. Alexander and Teitelbaum [2007] showed mountain waves in Antarctica resolved in ECMWF-T511, which were comparable with AIRS observations. The global distributions of GWs observed by MLS are similar to ECMWF-T799 results [Wu and Eckermann, 2008]. Encouraged by these results, our goal of this study is to investigate the temporal, spatial, and spectral dependence of GW variations during the 2009 SSW using ECMWF-T799. Lidar and COSMIC/GPS observations of GWs in the polar regions are also used to validate the GWs resolved by ECMWF-T799.

2. ECMWF-T799 and Comparisons With Lidar Data

[4] The ECMWF-T799 (hereafter referred to as ECMWF) analyses are derived from global four-dimensional assimilation of various atmospheric observations into the ECMWF model. Six-hourly output products have Δh of 0.25° and 91 vertical levels from the surface to 0.01 hPa. The vertical resolution Δz is ~ 0.4 km in the lower stratosphere and ~ 1 –2 km in the stratosphere (see Wu and Eckermann [2008] for discussion on ECMWF limitation). For this study, the ECMWF data are interpolated onto a regular 2-km vertical grid. To remove large scale waves such as tides and planetary waves, GW perturbations with zonal wavelength λ_u shorter than 2400 km and larger than 100 km ($4 \times \Delta h$) are extracted from temperature (T), zonal wind (U), meridional wind (V), and vertical wind (W) using wavelet analysis. GWs are further decomposed into five λ_u bands of 100–

¹High Altitude Observatory, National Center for Atmospheric Research, Boulder, Colorado, USA.

²Cooperative Institute for Research in Environmental Sciences and Department of Aerospace Engineering Sciences, University of Colorado at Boulder, Boulder, Colorado, USA.

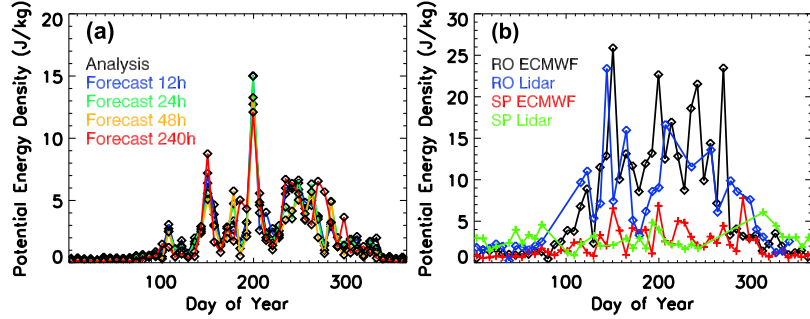


Figure 1. (a) The weekly-mean total GW-Ep at Rothera at 10 hPa for analysis and forecast versions with forecast hours of 12 h, 24 h, 48 h, and 240 h. (b) The weekly mean GW-Ep at Rothera (RO) in 2003–2005 and the South Pole (SP) in 1999–2001 obtained by lidar, compared with ECMWF in July 2008–June 2009 between 30–45 km. Every five other days of ECMWF data are used to obtain seasonal variations.

200 km, 200–400 km, 400–800 km, 800–1600 km, and 1600–2400 km ranges. For each band, GW-Ep [$\overline{E}_p = 1/2 (g/N)^2 (T'/T_0)^2$], and the vertical fluxes of zonal momentum ($\rho u' w'$) and meridional momentum ($\rho v' w'$) are calculated. Here T_0 is background temperature, T , u' , v' , and w' are perturbations of T, U, V, and W, respectively, N is the Brunt–Väisälä frequency, and g is the gravitational acceleration. The overbar indicates the spatial average over one

λ_u for $\rho v' w'$, $\rho u' w'$, and \overline{E}_p . Utilizing the relation of $\rho v' w' / \rho u' w' = l/k$ derived from the dispersion and polarization relations under the assumption of one dominant wave in each band, the horizontal wavenumber, h , is derived as

$$h = \sqrt{k^2 + l^2} = \sqrt{k^2 + \left[\left(\frac{\rho v' w'}{\rho u' w'} \right) k \right]^2} \quad (1)$$

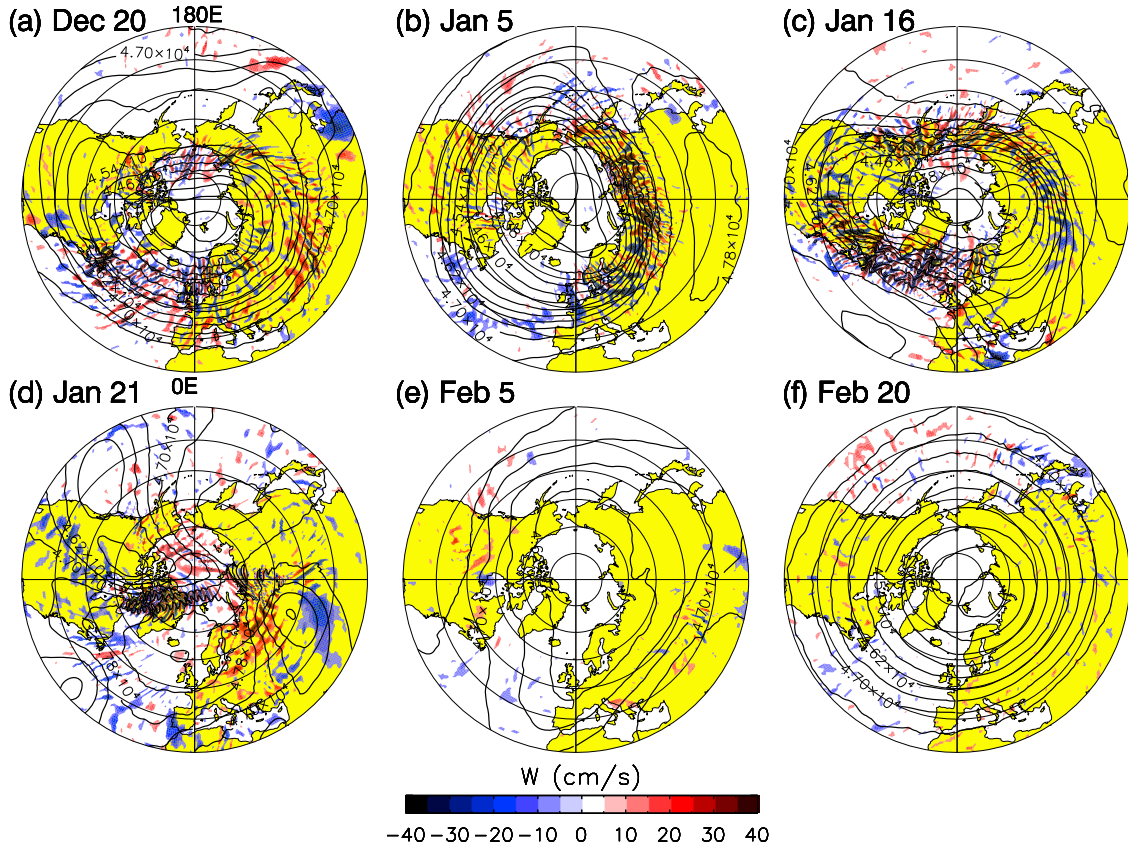


Figure 2. Filled and line contours represent the vertical wind (cm/s) and geopotential height (m), respectively, at 1 hPa on (a) Dec. 20, (b) Jan. 5, (c) Jan. 16, (d) Jan. 21, (e) Feb. 5, and (f) Feb. 20. Geopotential height line contour interval is 400 m. Only vertical winds larger than ± 8 cm/s are plotted. Continents are filled with yellow color.

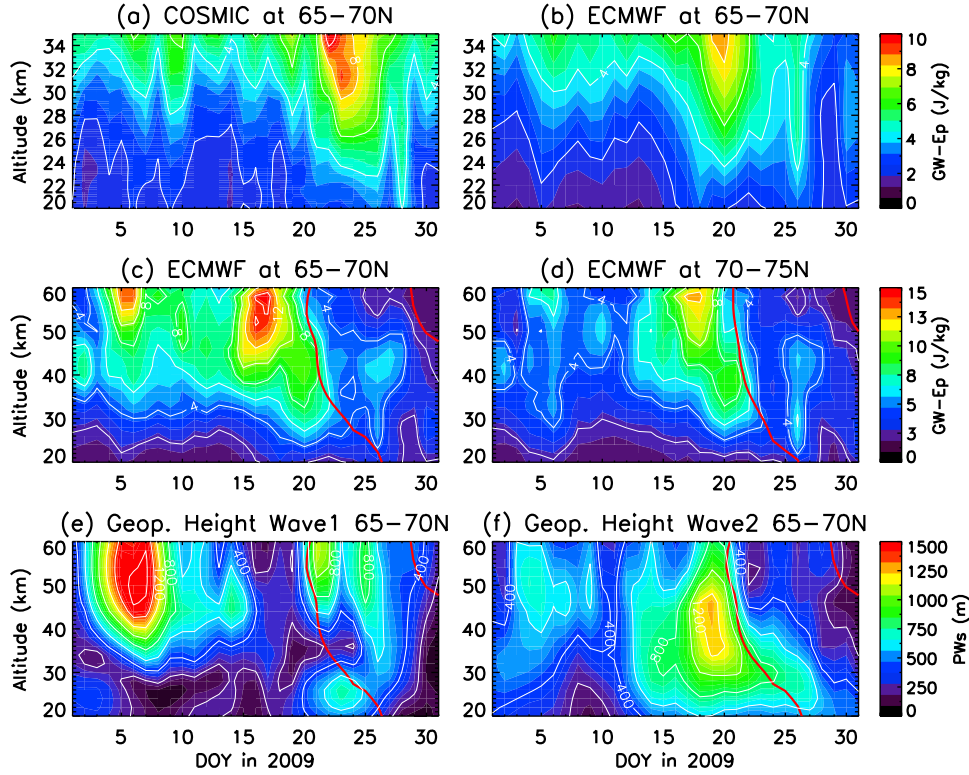


Figure 3. The daily-zonal mean total GW-Ep obtained by (a) COSMIC/GPS and (b) ECMWF at 65° – 70° N between 20–35 km and ECMWF at (c) 65° – 70° N and (d) 70° – 75° N between 20–60 km. The red lines are the zero zonal mean zonal wind line. The daily mean geopotential height amplitudes of (e) PW1 and (f) PW2 are plotted. A 10-km running mean is applied to ECMWF and COSMIC data.

where k and l are zonal and meridional wavenumbers, respectively. k is approximated according to each λ_u band of the wavelet analysis.

[5] Figure 1a compares the weekly mean GW-Ep obtained by the analysis and forecast versions of ECMWF from a one-year output. The forecast times are at 12, 24, 48, and 240 hours after initialization and the comparison is done at Rothera (67.5° S, 68.0° W) for the 10-hPa level. The magnitudes and variations of GW-Ep are comparable between the data sets, suggesting that the data assimilation process does not impart significant influences on GW. The analysis version will be used for the rest of this paper.

[6] Figure 1b shows the further comparisons of GW-Ep between ECMWF and available lidar observations from two Antarctic stations: the South Pole and Rothera, as reported by Yamashita *et al.* [2009]. Here, the ECMWF data were processed according to the lidar data processing approach. That is, GW-Ep is averaged over the altitude range of 30–45 km, rather than over one λ_u , to be consistent with lidar data analysis. Because of the 6-hourly ECMWF data, the mean background temperatures removed from actual temperature profiles are daily means in ECMWF, instead of the 3-hour means in lidar. This difference in background estimation and limitations in model resolution may lead to spectral coverage differences. Nevertheless, ECMWF properly captures the different seasonal variations observed by the lidars at these two stations: a large seasonal variation with a maximum in winter and a minimum in summer at Rothera and quiescent GW-Ep through the year at the South Pole. Such

favorable comparison further validates the ECMWF simulated GWs in the polar region.

3. Gravity Wave Variations During the 2009 SSW

[7] A major SSW is observed in the Arctic in January 2009. The temperature increases by ~ 50 K at 80° N and the zonal wind reversal occurs at 10 hPa on January 22–23 (the peak warming). At 1 hPa, the zonal wind reversal occurs on January 20–21, several days before the peak warming at 10 hPa. Figure 2 shows the polar plots of vertical wind (filled contours) and geopotential height (line contours) at 1 hPa in the Northern Hemisphere. The wave-1 geopotential height perturbation (PW1) occurs on January 5 when the significant, localized enhancement of GWs is seen between 45° – 135° E, where the background wind is the strongest. The wave-2 geopotential height perturbation (PW2) starts to grow on January 16, and the GW enhancements appear in two distinct locations 180° – 225° E and 300° – 360° E and correspond to the PW2 signature. By January 21, the polar vortex breaks down and GWs generally become weaker compared to Figures 2a–2c. As the polar vortex gradually recovers in February, GW presence nearly disappears and becomes significantly weaker than those on December 20 (before the SSW). ECMWF results show that the episodes of GW enhancements on January 5 and 16 correspond to regions of the strong background wind at the polar vortex edge which undergoes strong PW perturbations. As such, Figure 2 suggests that lidar observations would detect GW

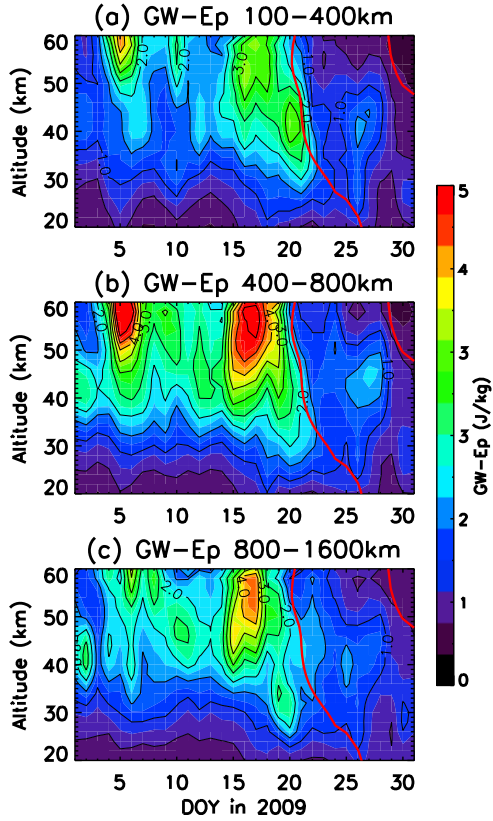


Figure 4. The daily-zonal mean ECMWF GW-Ep at 65° – 70° N in λ_h ranges of (a) 100–400 km, (b) 400–800 km, and (c) 800–1600 km. Red lines are the zero zonal mean zonal wind line.

enhancement or reduction during SSW, depending on the location of the lidar site relative to the locations of strong background wind at the polar vortex edge. This may explain the discrepancy of GWs reported previously by ground-based observations: the reductions [Whiteway and Carswell, 1994] and the enhancements [Duck et al., 1998] of GWs observed at the same location but in different years. As shown in Figures 3a–3d, the overall zonal-mean GW-Ep is enhanced during the SSW onset, consistent with satellite observations reported by Wang and Alexander [2009]. The locations of strong GWs are consistent with GEOS-5 assimilated data (V. Limpasuvan et al., Mesoscale simulations of gravity waves during the 2009 major stratospheric sudden warming, submitted to *Journal of Geophysical Research*, 2010), which further validates our GW analysis.

[8] Figures 3a and 3b show a comparison of the daily-zonal mean of total GW-Ep in January 2009 obtained from COSMIC/GPS and ECMWF. Detailed information of COSMIC/GPS is given by Wang and Alexander [2009, and references therein]. Temperature perturbations with the vertical wavelength less than 10 km are kept as GWs through high-pass filtering of COSMIC/GPS data [e.g., Venkat Ratnam et al., 2004]. GW-Ep amplitudes from the COSMIC/GPS are largest on January 21–25, around the peak warming. The magnitude of GW-Ep is slightly smaller in ECMWF than in COSMIC/GPS, and ECMWF shows the GW-Ep enhancement several days earlier than COSMIC/GPS. Despite these differences, the GW-Ep variation trends in ECMWF are generally comparable with COSMIC/GPS

observations. This comparison provides an additional validation of GWs resolved by ECMWF.

[9] To illustrate the altitude dependence of GWs, Figures 3c and 3d show the variations of daily-zonal mean GW-Ep in ECMWF between 20–60 km at 65° – 70° N and 70° – 75° N, respectively. The zero zonal-mean zonal wind line is overlaid on Figures 3c and 3d to indicate the wind reversal from eastward (on the left) to westward (on the right) and then recovery to eastward (at the far right). At 65° – 70° N, GW-Ep peaks on both January 5–7 and January 15–22. At 70° – 75° N GW-Ep in Figure 3d shows one peak only on January 15–22. In both latitude regions, the enhancement on January 15–22 first appears in the lower mesosphere on January 15 and then progresses down to the stratosphere. This downward progression seems to follow the wind reversal, and the GW-Ep enhancements occur well before the wind reversal at all altitudes. No significant GWs are observed after the wind reversal, which is consistent with HIRDLE observation [Wright et al., 2010].

[10] To further examine the correspondence between GW enhancement and PW growth, Figures 3e and 3f show PW1 and PW2 amplitudes at 65° – 70° N, respectively. Prior to the peak SSW, PW1 reaches a maximum around January 5, and GW-Ep increases at the same time. PW2 maximum occurs around January 20 shortly before the breakdown of the polar vortex and the wind reversal. The January 15–22 enhancement of GW-Ep corresponds to this episode of PW2. The PW disturbances in ECMWF are most significant in the lower mesosphere in the early stage of the 2009 SSW, and then progress to lower altitudes from January 5 to January 22, which is consistent with the study by Liu and Roble [2005]. The height differences of the maximum GW-Ep between January 5 and 20 seem to indicate the downward progression of GW enhancements corresponding to the downward progression of PWs.

[11] In contrast to GW-Ep at 65° – 70° N, GW-Ep at 70° – 75° N does not show a clear peak on January 5. This is likely because PW1 growth on January 5 is not strong enough and 70° – 75° N still lies within the polar vortex (where the wind is weak), resulting in the insignificant changes in GW-Ep at higher latitudes. On the other hand, PW2 growth displaces the polar vortex edge towards the pole and breaks the vortex on January 15–22. These results indicate the time lag of the GW-Ep enhancement between different latitudes depending on the movement of the polar vortex edge, which can also be seen in the polar plots of GWs in Figure 2. It should be pointed out that the application of Rayleigh friction above 1 hPa in ECMWF may cause some damping of GWs and weaken GWs above 1 hPa. Nevertheless, the relative changes of GWs during the 2009 SSW are still meaningful.

[12] To investigate the spectral dependence of GW responses to the 2009 SSW, GW-Ep is separated into the λ_h bands of 100–400 km, 400–800 km, and 800–1600 km, as shown in Figure 4. Two peaks on January 5 and January 15–22 exist in both 100–400 km and 400–800 km bands, and the magnitudes of GW-Ep in the 400–800 km band are two times larger than those in the 100–400 km band. GW-Ep in 800–1600 km shows a significant peak on January 16–18 but not on January 5. Two peaks on January 5 (the large PW1 event) and 15–22 (the large PW2 event) are dominated by 100–800 km band and 400–1600 km band, respectively. These results indicate the spectral dependence of GW-Ep enhancements and that GW may respond dif-

ferently to the different PW activities. It should be noted here that according to *Plougonven and Teitelbaum* [2003] the GWs resolved by ECMWF-T511 have different characteristics than those obtained from radiosonde observations at the same location and time. Although both Δh and Δz have been improved from T511 (0.5° and 61 vertical level) to T799 (0.25° and 91 vertical level), ECMWF-T799 could still have bias in resolving wave characteristics.

4. Conclusions

[13] The ECMWF-T799 data are used to identify GW variations during the 2009 SSW. ECMWF with Δh of 0.25° is capable of partially resolving mesoscale GWs with λ_u of ~ 100 km. The resolved GWs in the analysis and forecast versions of ECMWF show good agreements, indicating that data assimilation process does not result in significant spurious wave generation. The seasonal variations of ECMWF GW-Ep show a peak in winter at Rothera while no significant variations at the South Pole, which are consistent with the lidar observations.

[14] The ECMWF analyses show that most GWs occur at the edge of the polar vortex, and the magnitude and occurrence of GWs correlate with the location and strength of the polar vortex that is strongly distorted by PW growth. During the development and the onset of the SSW, the daily-zonal mean GW-Ep first increases on January 5 in coincidence with PW1 growth. Then, GW-Ep enhances again on January 15–22 as the PW2 magnifies. As the significant PW disturbances (initially at the lower mesosphere) migrate down to the stratosphere, strong GWs (also initially enhanced at higher altitudes on January 5) gradually progress downward to the stratosphere around January 22. The downward progression of GW-Ep and PW enhancement on January 15–22 seems to follow the zero-wind line. The two GW peaks on January 5 and 15–22 are dominated by 100–800 km band and 400–1600 km band, respectively, indicating the spectral dependence of GW enhancements. All of GW enhancements occur before the wind reversal, and GWs become significantly weak after the 2009 SSW. The overall GW-Ep variations in ECMWF are confirmed by COSMIC/GPS observations. The combination of ECMWF and COSMIC/GPS reveals the dependence of GW variations on location, altitude, time, and spectrum associated with SSWs.

[15] As pointed out by *Dunkerton* [1984], GWs show preferential propagation in regions with strong wind, and it may partially explain the ECMWF GW-Ep variations associated with SSWs. In addition, the dominant λ_h of 400–800 km from ECMWF is consistent with the sub-synoptic scales of GWs generated from flow adjustment (~ 600 km) [*O'Sullivan and Dunkerton*, 1995]. Mesoscale GWs are usually associated with topography, but can also be generated by flow adjustment [Zhang, 2004]. The spectral dependence may reflect the GW source influences on GW-Ep variations. The understanding of the physical mechanisms of GW variations is the basis of our future work.

[16] **Acknowledgments.** We acknowledge Walter Robinson and Varavut Limpasuvan for their valuable comments. We thank the ECMWF for

providing the data. C.Y. acknowledges NCAR Newkirk Graduate Fellowship. X.C. and C.Y. were partially supported by National Science Foundation (NSF) grants ANT-0839091 and ATM-0645584. H.L.L. is partially supported by the NSF CEDAR grants ATM-0535466 and ATM-0836386, and NASA LWS Strategic Capability (NNX09AJ83G). National Center for Atmospheric Research is sponsored by the NSF.

References

- Alexander, M. J., and H. Teitelbaum (2007), Observation and analysis of a large amplitude mountain wave event over the Antarctic peninsula, *J. Geophys. Res.*, **112**, D21103, doi:10.1029/2006JD008368.
- Duck, T. J., J. A. Whiteway, and A. I. Carswell (1998), Lidar observations of gravity wave activity and Arctic stratospheric vortex core warming, *Geophys. Res. Lett.*, **25**, 2813–2816, doi:10.1029/98GL02113.
- Dunkerton, T. J. (1984), Inertia-gravity waves in the stratosphere, *J. Atmos. Sci.*, **41**, 3396–3404, doi:10.1175/1520-0469(1984)041<3396:IWITS>2.0.CO;2.
- Kim, S.-Y., H.-Y. Chun, and D. L. Wu (2009), A study on stratospheric gravity waves generated by Typhoon Ewiniar: Numerical simulations and satellite observations, *J. Geophys. Res.*, **114**, D22104, doi:10.1029/2009JD011971.
- Liu, H.-L., and R. G. Roble (2002), A study of a self-generated stratospheric sudden warming and its mesospheric–lower thermospheric impacts using the coupled TIME-GCM/CCM3, *J. Geophys. Res.*, **107**(D23), 4695, doi:10.1029/2001JD001533.
- Liu, H.-L., and R. G. Roble (2005), Dynamical coupling of the stratosphere and mesosphere in the 2002 Southern Hemisphere major stratospheric sudden warming, *Geophys. Res. Lett.*, **32**, L13804, doi:10.1029/2005GL022939.
- O'Sullivan, D., and T. J. Dunkerton (1995), Generation of inertia-gravity waves in a simulated life cycle of baroclinic instability, *J. Atmos. Sci.*, **52**(21), 3695–3716, doi:10.1175/1520-0469(1995)052<3695:GOI-WIA>2.0.CO;2.
- Plougonven, R., and H. Teitelbaum (2003), Comparison of a largescale inertia-gravity wave as seen in the ECMWF analyses and from radiosondes, *Geophys. Res. Lett.*, **30**(18), 1954, doi:10.1029/2003GL017716.
- Schroeder, S., P. Preusse, M. Ern, and M. Riese (2009), Gravity waves resolved in ECMWF and measured by SABER, *Geophys. Res. Lett.*, **36**, L10805, doi:10.1029/2008GL037054.
- Venkat Ratnam, M., T. Tsuda, C. Jacobi, and Y. Aoyama (2004), Enhancement of gravity wave activity observed during a major Southern Hemisphere stratospheric warming by CHAMP/GPS measurements, *Geophys. Res. Lett.*, **31**, L16101, doi:10.1029/2004GL019789.
- Wang, L., and M. J. Alexander (2009), Gravity wave activity during stratospheric sudden warmings in the 2007–2008 Northern Hemisphere winter, *J. Geophys. Res.*, **114**, D18108, doi:10.1029/2009JD011867.
- Watanabe, S., Y. Kawatani, Y. Tomikawa, K. Miyazaki, M. Takahashi, and K. Sato (2008), General aspects of a T213L256 middle atmosphere general circulation model, *J. Geophys. Res.*, **113**, D12110, doi:10.1029/2008JD010026.
- Whiteway, J. A., and A. I. Carswell (1994), Rayleigh lidar observations of thermal structure and gravity wave activity in the high Arctic during a stratospheric warming, *J. Atmos. Sci.*, **52**(21), 3122–3136, doi:10.1175/1520-0469(1994)051<3122:RLOOTS>2.0.CO;2.
- Wright, C. J., S. M. Osprey, J. J. Barnett, L. J. Gray, and J. C. Gille (2010), High Resolution Dynamics Limb Sounder measurements of gravity wave activity in the 2006 Arctic stratosphere, *J. Geophys. Res.*, **115**, D02105, doi:10.1029/2009JD011858.
- Wu, D. L., and S. D. Eckermann (2008), Global gravity wave variances from Aura MLS: Characteristics and interpretation, *J. Atmos. Sci.*, **65**, 3695–3718, doi:10.1175/2008JAS2489.1.
- Yamashita, C., X. Chu, H.-L. Liu, P. J. Espy, G. J. Nott, and W. Huang (2009), Stratospheric gravity wave characteristics and seasonal variations observed by lidar at the South Pole and Rothera, Antarctica, *J. Geophys. Res.*, **114**, D12101, doi:10.1029/2008JD011472.
- Zhang, F. (2004), Generation of mesoscale gravity waves in upper-tropospheric jet-front systems, *J. Atmos. Sci.*, **61**, 440–457, doi:10.1175/1520-0469(2004)061<0440:GOMGWI>2.0.CO;2.

X. Chu and C. Yamashita, Cooperative Institute for Research in Environmental Sciences, University of Colorado at Boulder, 216 UCB, Boulder, CO 80309, USA. (chihoko.yamashita@colorado.edu)

H.-L. Liu, High Altitude Observatory, National Center for Atmospheric Research, PO Box 3000, Boulder, CO 80307, USA.